



Influence of Bi doping on physical properties of lead halide perovskites: a comparative first-principles study between CsPbI₃ and CsPbBr₃

Y. Kang ^{a,*}, S. Kang ^b, S. Han ^{b,**}

^a Materials Data Center, Korea Institute of Materials Science, Changwon, 51508, South Korea

^b Department of Materials Science and Engineering, Seoul National University, Seoul, 08826, South Korea

ARTICLE INFO

Article history:

Received 8 August 2019

Received in revised form

9 September 2019

Accepted 10 September 2019

Available online xxx

Keywords:

Lead halide perovskites

Doping

Defects

Density functional theory

ABSTRACT

We study the effects of Bi doping on the physical properties of CsPbX₃ (X = I or Br), promising active materials in application to the solar cell, using first-principles calculations with the hybrid functional. In both CsPbBr₃ and CsPbI₃, we find that excess electrons introduced by Bi replacing Pb (Bi_{Pb}) are mostly compensated by native acceptors such as Cs and Pb vacancies. As a result, the equilibrium Fermi level lies far below the defect level of Bi_{Pb}, indicating that Bi_{Pb} prefers the 1+ charge state over the neutral one. The band structure of Bi-doped CsPbX₃ shows that the interaction between the defect and host states affects the conduction band, narrowing the bandgap of the host material. The formation energy of Bi_{Pb} is smaller in CsPbI₃ than in CsPbBr₃, implying the easier doping of Bi in CsPbI₃. The computational results successfully explain distinct doping effects on absorption spectra between CsPbI₃ and CsPbBr₃, which was observed in recent experiments.

© 2019 The Authors. Published by Elsevier Ltd. This is an open access article under the CC BY-NC-ND license (<http://creativecommons.org/licenses/by-nc-nd/4.0/>).

1. Introduction

With outstanding optical and charge-transport properties, as well as solution processability, lead halide perovskites (LHPs) are emerging as a key component in low-cost and high-performance photovoltaic devices [1,2]. The power-conversion efficiency over 20% has been achieved by solar cells using the organic-inorganic hybrid LHPs such as CH₃NH₃PbI₃ (MAPI), HC(NH₂)₂PbI₃ (FAPI), and their mixed phases [3–5]. Recently, full-inorganic LHPs wherein Cs replaces the organic molecule are attracting attention because they exhibit superior environmental stability while their optoelectrical properties are on par with those of hybrid LHPs [6–9].

Doping with heterometal ions provides a route to tune the physical properties of LHPs, enabling performance enhancement in optoelectronic devices [10,11]. Diverse metal elements such as K, Rb, In, Sb, and Bi are being investigated as possible dopants [12–19]. Among them, the Bi dopant is found to replace Pb atoms in stable and controllable ways owing to similar ionic radii between Pb²⁺ and Bi³⁺ (1.19 and 1.03 Å, respectively) [8,12,14–16,18,19]. It

was found that Bi doping can enhance the efficiency of solar cells by increasing the visible-light absorption [16]. In addition, Bi doping was reported to enable a precise control of the charge transfer at the interface between LHPs and other materials by tuning the energy-level alignment [19].

In spite of the wide interest on Bi doping, understanding of doping effects on the physical properties of LHPs is still incomplete, which may impede optimizing the doping condition in various applications. For instance, Bi is a trivalent element that can serve as a donor when substituted for the Pb atom. Indeed, Hall effect or ultraviolet photoemission spectroscopy measurements showed an increase of the Fermi level of CH₃NH₃PbBr₃ (MAPB) and CsPbBr₃ films upon Bi doping [15,18,19]. However, the metallic conductivity was not observed even at high doping levels of 10¹⁹–10²¹ cm⁻³, and the Bi-doped films still behaved as semiconductors with the Fermi level near the midgap. Based on the first-principles calculations [20], it was claimed that the deep nature of substitutional Bi for the Pb site (Bi_{Pb}) was responsible for the semiconducting nature. As another explanation, the electrical compensation due to the formation of native acceptors was also suggested [18]. However, these two mechanisms have not been justified quantitatively, and thus, the origin of the limited conductivity of Bi-doped LHPs is still elusive. On the other hand, the absorption threshold of LHPs was

* Corresponding author.

** Corresponding author.

E-mail addresses: thehoya84@gmail.com (Y. Kang), hansw@snu.ac.kr (S. Han).

reported to shift toward lower frequencies under Bi doping. In MAPbBr₃ and CsPbBr₃, this redshift was attributed to the increase of tail states near band edges with the bandgap unaffected, although the origin of the absorption tail is not clear [14,15]. This contrasts with CsPbI₃ where the Bi doping resulted in redshifts of the absorption spectrum, i.e., bandgap narrowing, rather than the amplified tail states [16]. Such distinct effects of Bi doping on the absorption spectrum have not been explained clearly.

In this work, we address the aforementioned issues centered around Bi doping using the density functional theory (DFT) calculations. Among various competing polymorphs, the cubic phase of CsPbI₃ (α -CsPbI₃) and the orthorhombic phase of CsPbBr₃ (γ -CsPbBr₃) are chosen as the host material (see Fig. 1 for the crystal structures). Bi doping in both phases have been extensively studied in experiments [14–16,18,19]. While CsPbI₃ is stable in the orthorhombic phase (δ -CsPbI₃) at room temperatures, we select α -CsPbI₃ because it is receiving more attention in terms of practical applications [16]. We study effects of Bi doping on the electrical properties of CsPbX₃ ($X = \text{I or Br}$) by investigating the defect properties. Our calculations show that native acceptors such as Cs and Pb vacancies (V_{Cs} and V_{Pb} , respectively) substantially compensate n -type doping in both materials, suppressing the free-electron density to values far below the corresponding Bi_{Pb} concentration. As a result, the equilibrium Fermi level lies below Bi_{Pb} levels, implying that the 1+ charge state is the energetically favorable charge state of Bi_{Pb} . We analyze the band structure to obtain insights into doping-induced modification of the optical properties. The band structure of Bi-doped CsPbX₃ ($X = \text{I or Br}$) reveals that the conduction band of host materials becomes lower in energy than for the undoped cases, causing the redshift of the absorption onset. On the other hand, we find that the formation energy of Bi_{Pb} is smaller in α -CsPbI₃ than in γ -CsPbBr₃, indicating the easier doping of Bi in the former. Based on this fact, we shed light on the different absorption spectrum between Bi-doped CsPbI₃ and CsPbBr₃ observed in experiments.

2. Methods

2.1. DFT calculations

The present DFT calculations are carried out using the Vienna *Ab initio* Simulation Package (VASP) with projector-augmented wave

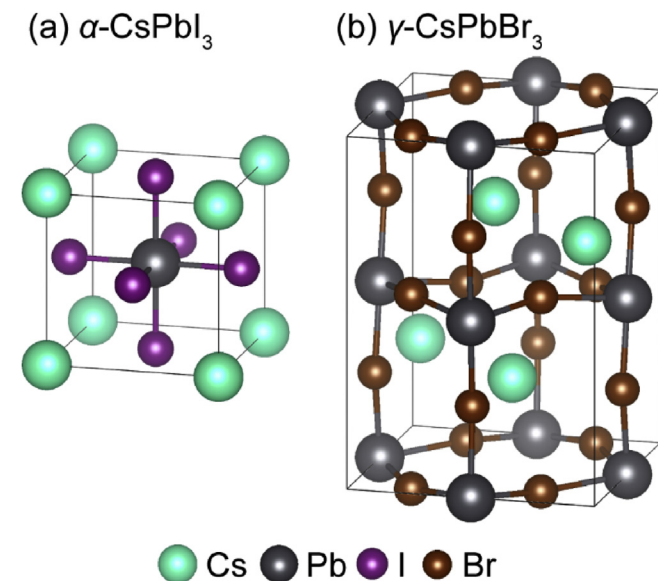


Fig. 1. Crystal structures of (a) α -CsPbI₃ and (b) γ -CsPbBr₃.

pseudopotentials [21,22]. A cutoff energy of 400 eV is used for expanding the plane-wave basis. Because of low computational cost and bandgaps similar to experimental values, the (semi)local functionals such as the Perdew–Burke–Ernzerh of functional [23], without the spin-orbit coupling (SOC) effect, have been used to examine defect properties of LHPs [24–27]. However, it was also noted that such an approach is limited in describing the defect properties accurately and that more elaborate methods such as hybrid functionals with the SOC should be used [28,29]. As such, we use the Heyd–Scuseria–Ernzerhof hybrid functional (HSE06) including SOC. The fraction of the exact Fock exchange was fitted to 0.76 and 0.55 for α -CsPbI₃ and γ -CsPbBr₃, respectively, to produce experimental bandgaps. All the atomic positions are optimized until magnitudes of atomic forces are reduced to within 0.05 eV/Å. The calculated fundamental properties such as the lattice parameters, bandgap, and heat of formation (ΔH^f) are listed in Table 1.

2.2. Defect formation energy

A $3 \times 3 \times 3$ supercell for α -CsPbI₃ (27 formula units of CsPbI₃) and a $2 \times 2 \times 2$ supercell for γ -CsPbBr₃ (32 formula units of CsPbBr₃) were used for the defect calculations. We sampled only the Γ -point for the Brillouin-zone integration. The defect formation energy (E^f) of a defect in the charge state q (D^q) was evaluated as [33].

$$E^f(D^q) = E_{\text{tot}}(D^q) - E_{\text{tot}}(\text{crystal}) - \sum_i N_i \mu_i + qE_F, \quad (1)$$

where $E_{\text{tot}}(D^q)$ and $E_{\text{tot}}(\text{crystal})$ are the total energy of a supercell with D^q and the perfect crystal, respectively, and E_F is the Fermi level with respect to the valence band maximum (VBM). For the formation energy of charged defects, the spurious interaction between periodic images was fixed by the monopole correction that considers the static dielectric constant of 20.5 measured in experiments [34]. We explicitly check the supercell size dependence of the formation energy with the example of $\text{Bi}_{\text{Pb}}^{1+}$ in α -CsPbI₃ and find that the formation energy changes by less than 0.1 eV when the $5 \times 5 \times 5$ supercell is used (Table S1). In Eq. (1), N_i is the number of type i atom removed from ($N_i < 0$) or added into ($N_i > 0$) the supercell and μ_i stands for its chemical potential. μ_i depends on the growth condition and should satisfy the following relation:

$$\mu_{\text{Cs}} + \mu_{\text{Pb}} + 3\mu_X = \Delta H^f(\text{CsPbX}_3). \quad (2)$$

To avoid the formation of competing binary phases, the following conditions are also imposed:

$$\mu_{\text{Cs}} + \mu_X \leq \Delta H^f(\text{CsX}), \quad (3)$$

$$\mu_{\text{Pb}} + 2\mu_X \leq \Delta H^f(\text{PbX}_2). \quad (4)$$

Fig. S1 depicts the stability region of each compound and corresponding chemical potentials. Note that α -CsPbI₃ is a metastable

Table 1

The calculated physical properties of α -CsPbI₃ and γ -CsPbBr₃. Experimental values are presented in parentheses.

Properties		α -CsPbI ₃	γ -CsPbBr ₃
Lattice parameter (Å)	a	6.28 (6.29 ³⁰)	8.29 (8.26 ³¹)
	b		11.80 (11.77 ³¹)
	c		8.22 (8.21 ³¹)
Bandgap (eV)		1.72 (1.73 ¹⁶)	2.26 (2.25–2.32 ^{15,32})
Heat of formation (eV/formula unit)		–6.20	–7.44

phase at low temperatures, and no chemical potentials ensure its phase stability against the other binary phases. In the present work, we considered the chemical potentials on the border line between the stable regions of CsI and PbI_2 for $\alpha\text{-CsPbI}_3$.

3. Results and discussion

3.1. Thermal ionization energies of Bi_{Pb}

Among possible sites for Bi in the CsPbX_3 crystal, we focus on Bi_{Pb} which was found to be more stable than other defects such as interstitials [12]. Fig. 2a shows the charge transition level between different charge states of Bi_{Pb} [$\epsilon(1+/0)$] obtained as $E^f(\text{Bi}_{\text{Pb}}^0) - E^f(\text{Bi}_{\text{Pb}}^{1+}; E_F = \text{VBM})$. This quantity corresponds to the thermodynamic defect level associated with the thermal ionization of Bi_{Pb} . It is seen in Fig. 2a that $\epsilon(1+/0)$ appears at 0.1 eV below the conduction band minimum (CBM) in $\alpha\text{-CsPbI}_3$ while 0.59 eV below the CBM in $\gamma\text{-CsPbBr}_3$ (the transition level of Bi_{Pb} for $\gamma\text{-CsPbBr}_3$ is in good agreement with previous HSE calculations) [12]. These ionization energies are much higher than the thermal energy at room temperatures (~ 0.025 eV). Thus, only a small portion of doped Bi_{Pb}

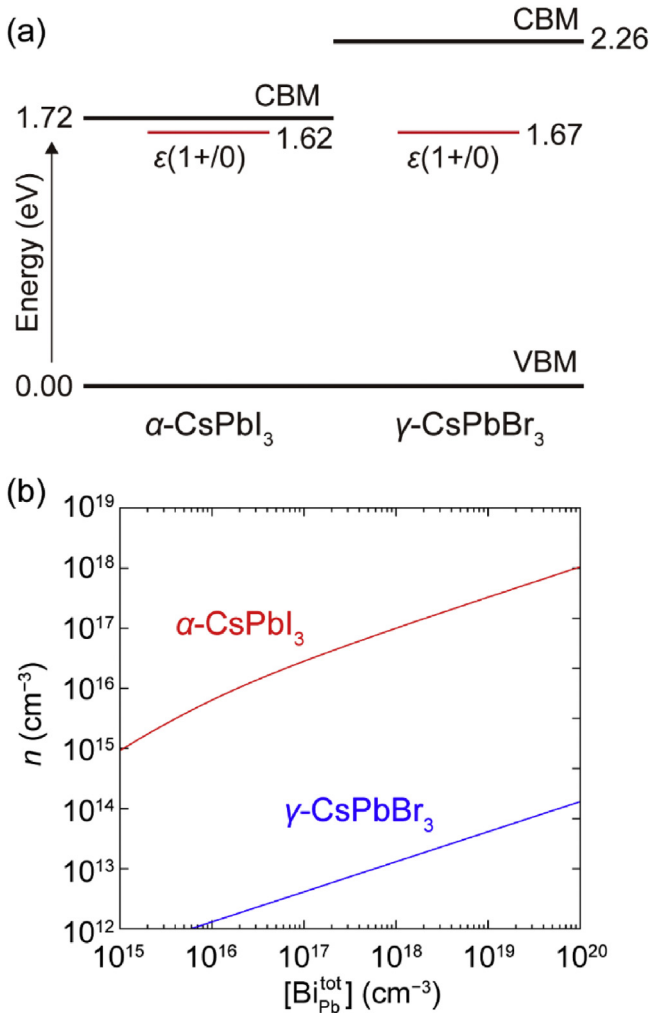


Fig. 2. (a) The charge transition level of Bi_{Pb} in $\alpha\text{-CsPbI}_3$ and $\gamma\text{-CsPbBr}_3$. The VBM of each material is set to 0. (b) The equilibrium free-electron concentration (n) satisfying the charge neutrality condition of $\alpha\text{-CsPbI}_3$ (red line) and $\gamma\text{-CsPbBr}_3$ (blue line) as a function of the Bi doping concentration ($[\text{Bi}_{\text{Pb}}^{\text{tot}}]$) without considering the effect of other defects. CBM, conduction band maximum; VBM, valence band maximum.

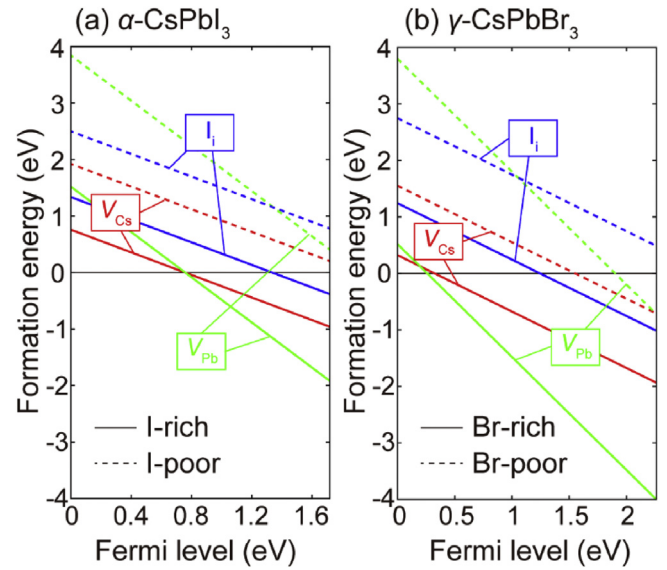


Fig. 3. The formation energies of V_{Cs}^{1-} , V_{Pb}^{2-} , and I_i^{1-} as a function of Fermi level in (a) $\alpha\text{-CsPbI}_3$ and (b) $\gamma\text{-CsPbBr}_3$.

is expected to be ionized at the room temperature. To explicitly obtain how many carriers are generated owing to Bi doping, we calculate the equilibrium concentration of free electrons (n) by imposing the charge neutrality condition, $n = [\text{Bi}_{\text{Pb}}^{1+}]$, where $[\text{Bi}_{\text{Pb}}^{1+}]$ is the concentration of ionized donors, neglecting influences of other defects (see details for the calculation of the equilibrium concentration in Supporting Information). n also relates to the Fermi level as follows:

$$n = N_C \exp\left(\frac{E_F - \text{CBM}}{kT}\right), \quad (5)$$

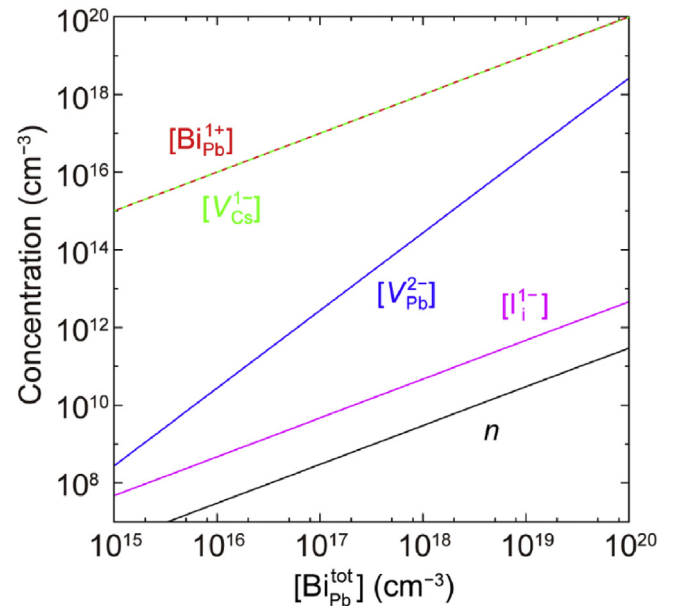


Fig. 4. The equilibrium concentration of the free electron and defects ($\text{Bi}_{\text{Pb}}^{1+}$, V_{Cs}^{1-} , V_{Pb}^{2-} , and I_i^{1-}) satisfying the charge neutrality condition in $\alpha\text{-CsPbI}_3$ at 300 K. For the formation energy of the compensators, we consider the intermediate growth condition and assume that their concentrations are quenched as the one equilibrated at annealing temperature (see main text).

where N_C is the effective density of states for the conduction band, k the Boltzmann constant, and T the temperature. For N_C , we use the calculated effective mass of 0.12 and 0.20 m_e for α -CsPbI₃ and γ -CsPbBr₃, respectively. The dependence of $[Bi_{Pb}^{1+}]$ on the Fermi level is given by the following equation [35].

$$[Bi_{Pb}^{1+}] = \frac{[Bi_{Pb}^{tot}]}{1 + 2\exp\left\{\frac{E_F - \epsilon(1+/0)}{kT}\right\}}, \quad (6)$$

where $[Bi_{Pb}^{tot}]$ is the total Bi concentration (cumulated over the charge state). The equilibrium $[Bi_{Pb}^{tot}]$ can be computed from the formation energy of Bi_{Pb} , but this requires information on the Bi chemical potential which may reflect the actual growth condition. Thus, for simplicity, we use $[Bi_{Pb}^{tot}]$ as the variable. Fig. 2b illustrates that most of Bi_{Pb} in α -CsPbI₃ is ionized, generating as many n as the dopant concentration at $[Bi_{Pb}^{tot}] \sim 10^{15} \text{ cm}^{-3}$. The ionization efficiency gradually decreases with increasing $[Bi_{Pb}^{tot}]$, and only 1% of $[Bi_{Pb}^{tot}]$

contributes to the free-carrier concentration when $[Bi_{Pb}^{tot}]$ reaches 10^{20} cm^{-3} (2.44% of the Bi/Pb ratio). Such inefficient ionization at high doping concentrations is caused by the shift of the Fermi level toward higher energy, which increases the energy cost for adding electrons to the host material. According to n in Fig. 2b, when a few percent of Bi is doped in the α -CsPbI₃ film, its resistivity is expected to decrease dramatically by several orders of magnitudes in comparison with the undoped film. However, the actual reduction in the resistance was measured to be less than two orders of magnitude when the Bi/Pb ratio ranges over 2.57–11.94% [16]. A similar discrepancy between theory and experiment is found for γ -CsPbBr₃; n is calculated to be slightly higher than 10^{14} cm^{-3} at $[Bi_{Pb}^{tot}] = 10^{20} \text{ cm}^{-3}$ (the Bi/Pb atomic ratio of 2.05%) for which the equilibrium E_F lies at 0.25 eV below the CBM. In experiment, by contrast, the Fermi level is located below the midgap in CsPbBr₃ with 2% of the Bi/Pb ratio [19]. Therefore, we conclude that the deep nature of Bi_{Pb} is not the main origin for the absence of n -type conductivity of Bi-doped CsPbX₃ found in experiments.

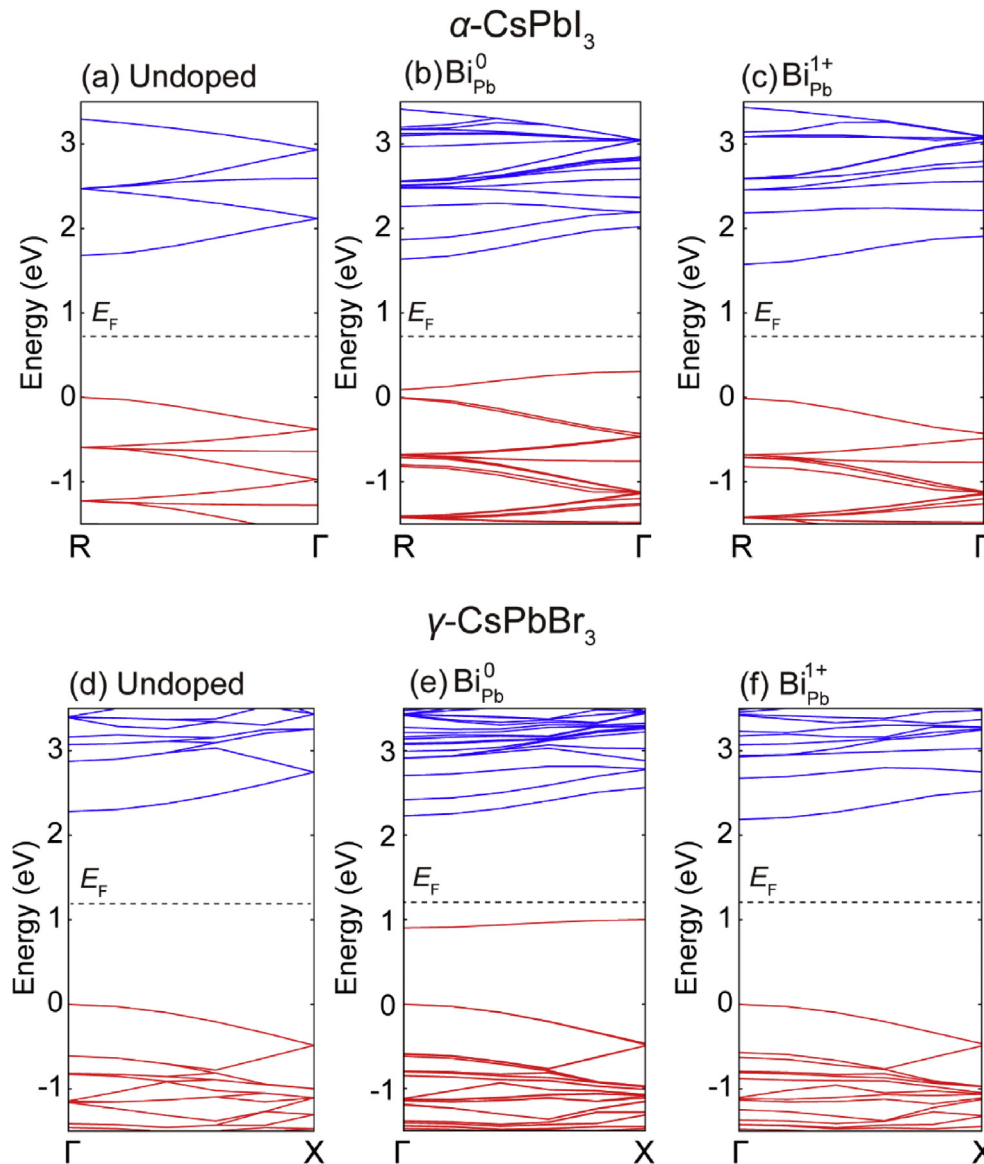


Fig. 5. The band structure of (a) undoped, (b) Bi_{Pb}^0 -doped, and (c) Bi_{Pb}^{1+} -doped α -CsPbI₃. The band structure of (e) undoped, (f) Bi_{Pb}^0 -doped, and (g) Bi_{Pb}^{1+} -doped γ -CsPbBr₃.

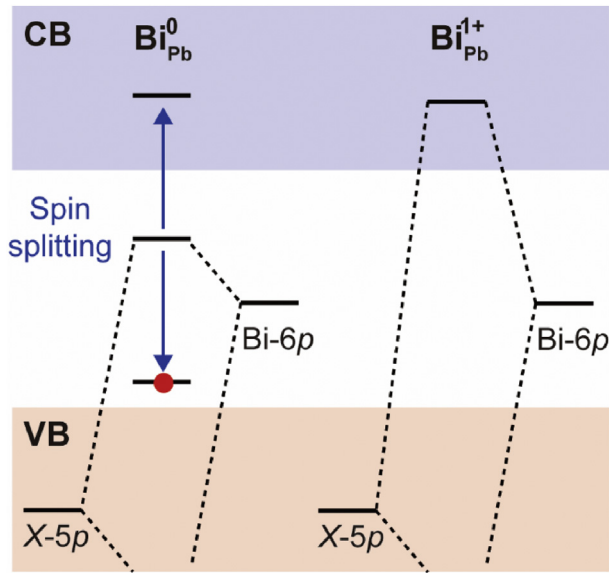


Fig. 6. Interaction between Bi and X-p states depending on the charge state of Bi_{p_b}. CB, conduction band; VB, valence band.

Table 2

The bond length (in unit of Å) of Pb-X and Bi-X in α -CsPbI₃ and γ -CsPbBr₃.

	Pb-X	Bi-X	
		Bi _{p_b} ⁰	Bi _{p_b} ¹⁺
α -CsPbI ₃	3.19	3.20	3.07
γ -CsPbBr ₃	2.98	2.98	2.84

3.2. Carrier compensation due to native acceptors

Next, we discuss the effect of native acceptors on the carrier compensation. Three types of point defects, V_{Cs}^{1-} , V_{Pb}^{2-} , and X interstitial in the 1- charge state (X_i^{1-}), are considered as potential compensating centers. (V_{Pb}^{1-} was reported to have the higher formation energy than V_{Pb}^{2-} , and thus, we do not consider it in the present work.) [36] It was reported that Bi_{p_b} itself may contribute to the compensation of free electrons by forming the DY center [37], which is neglected in this work, but its impact is expected to be negligible because of the higher formation energy compared with those of native acceptors [38]. In Fig. 3, we plot the formation energy of these defects with respect to the Fermi level under the X-rich or X-poor growth conditions. (Corresponding chemical potentials are shown in Fig. S1.) The upper limit of the Fermi level in Fig. 3 corresponds to the bandgap of each material. The slope of the formation energy curve of a given defect reflects its charge state.

In α -CsPbI₃, the formation energies of the compensating defects are relatively small [Fig. 3a], implying the difficulty in electron doping. To be specific, V_{Cs}^{1-} and V_{Pb}^{2-} at the I-rich condition have the negative formation energies when the Fermi level is above 0.75 eV. As a result, the equilibrium Fermi level satisfying the charge neutrality cannot be larger than 0.75 eV for this growth condition, which means that n-type doping is not feasible. The formation energy of every compensator increases as the growth environment evolves from the I-rich to I-poor condition, and for the latter case, all the defects have the positive formation energies for the entire range of the Fermi level. Nevertheless, the formation energies still remain low. In particular, the formation energy of V_{Cs}^{1-} becomes

smaller than 1 eV when the Fermi level is higher than 0.92 eV. This means that carrier compensation can occur significantly.

We assess the carrier compensation by these native defects quantitatively by evaluating n explicitly. As in the aforementioned case, we apply the charge neutrality condition, but in this case, the presence of the compensators is taken into account as $n + [V_{Cs}^{1-}] + 2 \times [V_{Pb}^{2-}] + [I_i^{1-}] = [Bi_{p_b}^{1+}]$. The concentration of the native defects is calculated by

$$[D^q] = N_s \exp \left\{ - \frac{E^f(D^q)}{kT} \right\}, \quad (7)$$

where N_s is the density of defect sites. The extreme growth conditions assumed in the aforementioned case may not reflect the experimental situation properly. Herein, we consider the intermediate growth condition for the defect formation energy. (See the chemical potential for this condition in Fig. S1.) We assume that the concentration of the native defects is quenched similar to those in high-temperature annealing [39,40]. That is to say, we initially set the temperature to 373 K, the annealing temperature in experiments [16], and obtain the equilibrium concentrations of the compensators. Then, we recalculate n at 300 K by retaining the concentrations of compensators equilibrated at 373 K. Fig. 4 shows that n for Bi-doped CsPbI₃ is highly suppressed when the carrier compensation by the native acceptors is taken into account; [Bi] of 10^{20} cm^{-3} leads to n less than 10^{12} cm^{-3} that is six orders of magnitudes smaller than the one without carrier compensation. This result implies that the conductivity cannot increase by the amount of the Bi density. Indeed, 4% Bi doping leads to the decrease of the resistance of films only by two orders of magnitude [16]. The most critical compensator is found to be V_{Cs}^{1-} whose concentration is almost the same as $[Bi_{p_b}^{1+}]$. We note that the equilibrium Fermi level in Bi-doped CsPbI₃ is located far below the defect level of Bi_{p_b}, and thus, Bi_{p_b} predominantly exists in the 1+ charge state. This again supports the conclusion drawn in the previous section that the deep nature of Bi_{p_b} is not responsible for the low n-type conductivity in experiments.

The carrier compensation by native acceptors is likely to be more significant in γ -CsPbBr₃, as inferred by the lower formation energy of the compensators (Fig. 3). In fact, n in Bi-doped CsPbBr₃ is calculated to be negligible with $[Bi_{p_b}^{tot}]$ up to 10^{20} cm^{-3} when considering the carrier compensation. This means that the equilibrium Fermi level is located below the midgap in Bi-doped CsPbBr₃, which agrees with experimental measurements [19]. As a result, Bi_{p_b} is completely ionized in γ -CsPbBr₃, as in α -CsPbI₃. Overall, in light of these results, Bi_{p_b} acts as donors, but Bi incorporation does not alter the electrical properties of CsPbX₃ significantly because of the carrier compensation of the native acceptors.

3.3. Impact of Bi_{p_b} on the absorption properties

We find that the alternation of the absorption properties upon Bi doping is associated with the doping-induced modification of the electronic band structure. Fig. 5a–c compare the band structures of the undoped, Bi_{p_b}⁰-doped, and Bi_{p_b}¹⁺-doped supercells of α -CsPbI₃, respectively. For Bi_{p_b}⁰, an occupied defect level is seen in the bandgap at 0.25 eV above the VBM. This defect state develops through antibonding between Bi-6p and neighboring I-5p states. (The corresponding bonding state lies far below the VBM.) To note, the defect state is singly occupied by an electron with a certain spin direction, while the corresponding unoccupied spin state is located above the conduction band because of spin-splitting effects, as depicted in Fig. 6. Once Bi_{p_b}¹⁺ forms with an electron removed from the defect level, the bonds between Bi and neighboring I atoms

become shortened (see Table 2 for the Bi-I bond length with respect to the charge state of Bi_{Pb}), stabilizing the occupied bonding state. This change in the Bi-I bond length raises the antibonding state above the conduction band owing to the enhanced bonding-antibonding splitting, as illustrated in Fig. 6. We note that the lowest conduction band for $\text{Bi}_{\text{Pb}}^{1+}$, which is preferred over Bi_{Pb}^0 , downshifts in energy compared with the undoped crystal. This is attributed to the interaction of host states with the unoccupied defect state. As a result, the bandgap is narrowed. The bandgap reduction due to the presence of $\text{Bi}_{\text{Pb}}^{1+}$ is found to be 0.15 eV when the doping concentration is $1.52 \times 10^{20} \text{ cm}^{-3}$ (the Bi/Pb ratio of 3.85%). This is in good agreement with the 0.17-eV redshift in absorption onset that was experimentally measured for $\alpha\text{-CsPbI}_3$ films including the Bi/Pb ratio of 4.22% [16]. This implies that the alternation of the conduction band caused by the electrostatic influence of $\text{Bi}_{\text{Pb}}^{1+}$ is the main origin of the redshift in the absorption spectrum.

In $\gamma\text{-CsPbBr}_3$, the atomic (Table 2) and electronic structures (Fig. 5d–f) vary depending on the charge state of Bi_{Pb} , which is similar to $\alpha\text{-CsPbI}_3$; the defect state with the antibonding character is found inside the bandgap for Bi_{Pb}^0 , while it shifts above the conduction band when $\text{Bi}_{\text{Pb}}^{1+}$ forms. As found in $\alpha\text{-CsPbI}_3$, the bandgap reduces by 0.09 eV in the presence of $\text{Bi}_{\text{Pb}}^{1+}$ with the concentration of $1.55 \times 10^{20} \text{ cm}^{-3}$ (the Pb/Bi ratio of 3.23%). However, photoluminescence and spectroscopic ellipsometry supported that the bandgap of Bi-doped CsPbBr_3 does not change significantly. Rather, tail states below the gap increased, changing the color of crystals from yellowish orange to dark red with the increasing dopant density [14,15]. The absorption tail would be attributed to the small Bi concentration in $\gamma\text{-CsPbBr}_3$; the CBM would alter locally at low doping concentrations (Fig. 7a), causing the tail-like absorption below the gap (Fig. 7b). In contrast, the gap variation would be smooth over the whole crystal at the high doping density (Fig. 7c), leading to the noticeable shift in the absorbance (Fig. 7d).

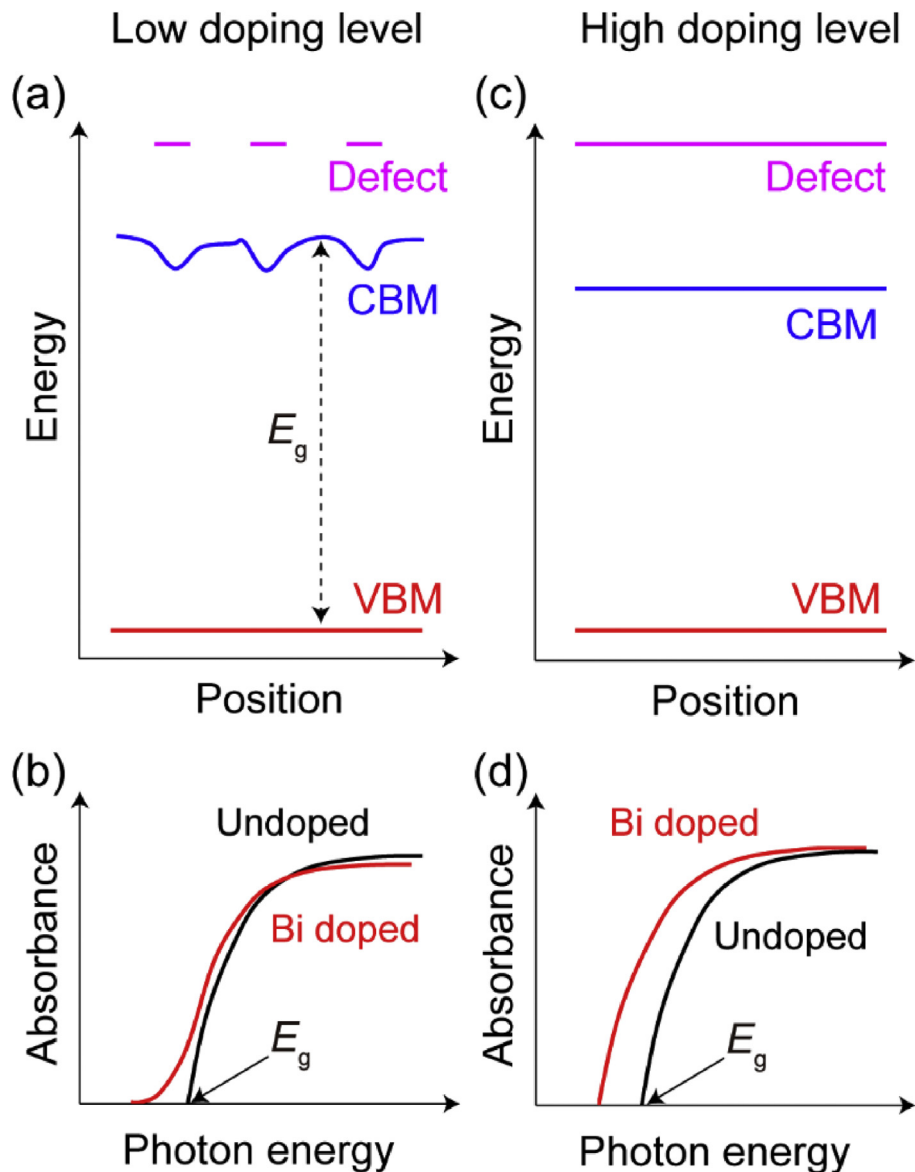


Fig. 7. Schematic band diagram for low (a) and high (c) doping level of Bi_{Pb} . Expected absorbance as a function of photon energy is shown in (b) for low and (d) for high doping level. CBM, conduction band maximum; VBM, valence band maximum.

Indeed, the doping concentration of Bi was one or two orders of magnitude smaller in CsPbBr₃ in reference to CsPbI₃ although both materials were synthesized under similar solution-based processes [15,16]. This can be explained by the defect energies; the formation energy of Bi_{Pb}¹⁺ is lower in α -CsPbI₃ than in γ -CsPbBr₃ by 0.15 eV when the Fermi level is near the midgap. (Bi-rich and BiX₃ phases are considered in determining the chemical potentials of Bi and Pb). This indicates that Bi doping is more facile in α -CsPbI₃ than in γ -CsPbBr₃, which is consistent with the experiment.

In passing, we remark on influences of other defects on the absorption properties of Bi-doped CsPbX₃. We find that V_{Cs}¹⁻, the major compensator, lowers the VBM and hence increases the bandgap of the γ -CsPbBr₃ model by 0.1 eV. Experimentally, however, the VBM of this material was unaffected by Bi doping [15]. Such discrepancy might be caused by other defects that are not considered in the present work, and further investigation is in demand.

4. Conclusion

We investigated the defect properties and electronic structures of Bi-doped CsPbX₃. The present results support that free electrons of Bi-doped CsPbX₃ are significantly compensated by the formation of native acceptors. In addition, we found that Bi_{Pb} predominantly exists in the 1+ charge state in the CsPbX₃ crystals, lowering the conduction band. As a result, Bi doping can contribute to the redshift of absorption onset found in experiments. Finally, based on the formation energy of Bi_{Pb}, we provided a plausible explanation on the difference in the doping-induced change of absorption spectrum between α -CsPbI₃ and γ -CsPbBr₃. By unveiling the impacts of Bi doping on the physical properties of CsPbX₃, this work will help improve the device performance using LHPs with doping. Furthermore, this work will serve as a useful reference for future defect studies on LHPs using first-principles calculations.

Conflict of interest

The authors declare that they have no known competing financial interests or personal relationships that could have appeared to influence the work reported in this article.

Acknowledgments

This work was supported by Creative Materials Discovery Program by the National Research Foundation of Korea (2017M3D1A1040689). Y. Kang acknowledges the Fundamental Research Program (PNK6410) of the Korea Institute of Materials Science, Republic of Korea.

Appendix A. Supplementary data

Supplementary data to this article can be found online at <https://doi.org/10.1016/j.mtadv.2019.100019>.

References

- [1] M.A. Green, A. Ho-Baillie, H.J. Snaith, The emergence of perovskite solar cells, *Nat. Photonics* 8 (7) (2014) 506–514.
- [2] S.D. Stranks, H.J. Snaith, Metal-halide perovskites for photovoltaic and light-emitting devices, *Nat. Nanotechnol.* 10 (5) (2015) 391–402.
- [3] M.A. Green, E.D. Dunlop, D.H. Levi, J. Hohl-Ebinger, M. Yoshita, A.W.Y. Ho-Baillie, Solar cell efficiency tables (version 54), *Prog. Photovolt. Res. Appl.* 27 (7) (2019) 565–575.
- [4] C.H. Chiang, M.K. Nazeeruddin, M. Gratzel, C.G. Wu, The synergistic effect of H₂O and DMF towards stable and 20% efficiency inverted perovskite solar cells, *Energy Environ. Sci.* 10 (3) (2017) 808–817.
- [5] D.Q. Bi, W. Tress, M.I. Dar, P. Gao, J.S. Luo, C. Renevier, K. Schenk, A. Abate, F. Giordano, J.P.C. Baena, J.D. Decoppet, S.M. Zakeeruddin, M.K. Nazeeruddin, M. Gratzel, A. Hagfeldt, Efficient luminescent solar cells based on tailored mixed-cation perovskites, *Sci. Adv.* 2 (1) (2016) e1501170.
- [6] Y. Kang, S. Han, Intrinsic carrier mobility of cesium lead halide perovskites, *Phys. Rev. Appl.* 10 (4) (2018) 044013.
- [7] M.I. Saidaminov, M.A. Haque, J. Almutlaq, S. Sarmah, X.H. Miao, R. Begum, A.A. Zhumekenov, I. Dursun, N. Cho, B. Murali, O.F. Mohammed, T. Wu, O.M. Bakr, Inorganic lead halide perovskite single crystals: phase-selective low-temperature growth, carrier transport properties, and self-powered photodetection, *Adv. Opt. Mater.* 5 (2) (2017) 1600704.
- [8] X.L. Miao, T. Qiu, S.F. Zhang, H. Ma, Y.Q. Hu, F. Bai, Z.C. Wu, Air-stable CsPb_{1-x}Bi_xBr₃ (0 <= x << 1) perovskite crystals: optoelectronic and photostriction properties, *J. Mater. Chem. C* 5 (20) (2017) 4931–4939.
- [9] M. Kulbak, S. Gupta, N. Kedem, I. Levine, T. Bendikov, G. Hodes, D. Cahen, Cesium enhances long-term stability of lead bromide perovskite-based solar cells, *J. Phys. Chem. Lett.* 7 (1) (2016) 167–172.
- [10] Y. Zhou, J. Chen, O.M. Bakr, H.T. Sun, Metal-doped lead halide perovskites: synthesis, properties, and optoelectronic applications, *Chem. Mater.* 30 (19) (2018) 6589–6613.
- [11] Y.Y. Zhou, Z.M. Zhou, M. Chen, Y.X. Zong, J.S. Huang, S.P. Pang, N.P. Padture, Doping and alloying for improved perovskite solar cells, *J. Mater. Chem. A* 4 (45) (2016) 17623–17635.
- [12] J. Yin, G.H. Ahmed, O.M. Bakr, J.L. Bredas, O.F. Mohammed, Unlocking the effect of trivalent metal doping in all-inorganic CsPbBr₃ perovskite, *ACS Energy Lett.* 4 (3) (2019) 789–795.
- [13] W.G. Zhao, Z. Yao, F.Y. Yu, D. Yang, S.Z. Liu, Alkali metal doping for improved CH₃NH₃PbI₃ perovskite solar cells, *Adv. Sci.* 5 (2) (2018) 1700131.
- [14] P.K. Nayak, M. Sendner, B. Wenger, Z.P. Wang, K. Sharma, A.J. Ramadan, R. Lovrincic, A. Pucci, P.K. Madhu, H.J. Snaith, Impact of Bi³⁺ heterovalent doping in organic-inorganic metal halide perovskite crystals, *J. Am. Chem. Soc.* 140 (2) (2018) 574–577.
- [15] O.A. Lozhkina, A.A. Murashkina, V.V. Shilovskikh, Y.V. Kapitonov, V.K. Ryabchuk, A.V. Emeline, T. Miyasaka, Invalidity of band-gap engineering concept for Bi³⁺ heterovalent doping in CsPbBr₃ halide perovskite, *J. Phys. Chem. Lett.* 9 (18) (2018) 5408–5411.
- [16] Y.Q. Hu, F. Bai, X.B. Liu, Q.M. Ji, X.L. Miao, T. Qiu, S.F. Zhang, Bismuth incorporation stabilized α -CsPbI₃ for fully inorganic perovskite solar cells, *ACS Energy Lett.* 2 (10) (2017) 2219–2227.
- [17] M. Saliba, T. Matsui, K. Domanski, J.Y. Seo, A. Ummadisingu, S.M. Zakeeruddin, J.P. Correa-Baena, W.R. Tress, A. Abate, A. Hagfeldt, M. Gratzel, Incorporation of rubidium cations into perovskite solar cells improves photovoltaic performance, *Science* 354 (6309) (2016) 206–209.
- [18] A.L. Abdelhady, M.I. Saidaminov, B. Murali, V. Adinolfi, O. Voznyy, K. Katsiev, E. Alarousu, R. Comin, I. Dursun, L. Sinatra, E.H. Sargent, O.F. Mohammed, O.M. Bakr, Heterovalent dopant incorporation for bandgap and type engineering of perovskite crystals, *J. Phys. Chem. Lett.* 7 (2) (2016) 295–301.
- [19] R. Begum, M.R. Parida, A.L. Abdelhady, B. Murali, N.M. Alyami, G.H. Ahmed, M.N. Hedhili, O.M. Bakr, O.F. Mohammed, Engineering interfacial charge transfer in CsPbBr₃ perovskite nanocrystals by heterovalent doping, *J. Am. Chem. Soc.* 139 (2) (2017) 731–737.
- [20] E. Mosconi, B. Merabet, D. Meggiolaro, A. Zaoui, F. De Angelis, First-principles modeling of bismuth doping in the MAPbI₃ Perovskite, *J. Phys. Chem. C* 122 (25) (2018) 14107–14112.
- [21] G. Kresse, D. Joubert, From ultrasoft pseudopotentials to the projector augmented-wave method, *Phys. Rev. B* 59 (1999) 1758–1775.
- [22] G. Kresse, J. Furthmüller, Efficient iterative schemes for ab initio total-energy calculations using a plane-wave basis set, *Phys. Rev. B* 54 (1996) 11169.
- [23] J.P. Perdew, K. Burke, M. Ernzerhof, Generalized gradient approximation made simple, *Phys. Rev. Lett.* 77 (1996) 3865.
- [24] N. Liu, C.Y. Yam, First-principles study of intrinsic defects in formamidinium lead triiodide perovskite solar cell absorbers, *Phys. Chem. Chem. Phys.* 20 (10) (2018) 6800–6804.
- [25] W.J. Yin, T.T. Shi, Y.F. Yan, Unusual defect physics in CH₃NH₃PbI₃ perovskite solar cell absorber, *Appl. Phys. Lett.* 104 (6) (2014) 063903.
- [26] M.L. Agiorgousis, Y.Y. Sun, H. Zeng, S.B. Zhang, Strong Covalency-Induced recombination centers in perovskite solar cell material CH₃NH₃PbI₃, *J. Am. Chem. Soc.* 136 (41) (2014) 14570–14575.
- [27] J. Kim, S.H. Lee, J.H. Lee, K.H. Hong, The role of intrinsic defects in methylammonium lead iodide perovskite, *J. Phys. Chem. Lett.* 5 (8) (2014) 1312–1317.
- [28] D. Meggiolaro, F. De Angelis, First-principles modeling of defects in lead halide perovskites: best practices and open issues, *ACS Energy Lett.* 3 (9) (2018) 2206–2222.
- [29] M.H. Du, Density functional calculations of native defects in CH₃NH₃PbI₃: effects of spin-orbit coupling and self-interaction error, *J. Phys. Chem. Lett.* 9 (14) (2018), 3799–3799.
- [30] D.M. Trots, S.V. Myagkota, High-temperature structural evolution of caesium and rubidium triiodoplumbates, *J. Phys. Chem. Solids* 69 (10) (2008) 2520–2526.
- [31] P. Cottingham, R.L. Brutchey, On the crystal structure of colloiddally prepared CsPbBr₃ quantum dots, *Chem. Commun.* 52 (30) (2016) 5246–5249.
- [32] C.C. Stoumpos, C.D. Malliakas, J.A. Peters, Z.F. Liu, M. Sebastian, J. Im, T.C. Chasapis, A.C. Wibowo, D.Y. Chung, A.J. Freeman, B.W. Wessels, M.G. Kanatzidis, Crystal growth of the perovskite semiconductor CsPbBr₃: a new material for high-energy radiation detection, *Cryst. Growth Des.* 13 (7) (2013) 2722–2727.

- [33] C. Freysoldt, B. Grabowski, T. Hickel, J. Neugebauer, G. Kresse, A. Janotti, C.G. Van de Walle, First-principles calculations for point defects in solids, *Rev. Mod. Phys.* 86 (1) (2014) 253–305.
- [34] J.N. Wilson, J.M. Frost, S.K. Wallace, A. Walsh, Dielectric and ferroic properties of metal halide perovskites, *Apl. Mater.* 7 (1) (2019) 010901.
- [35] A.T. Neal, S. Mou, R. Lopez, J.V. Li, D.B. Thomson, K.D. Chabak, G.H. Jessen, Incomplete ionization of a 110 meV unintentional donor in β -Ga₂O₃ and its effect on power devices, *Sci. Rep.* 7 (2017) 13218.
- [36] J. Kang, L.W. Wang, High defect tolerance in lead halide perovskite CsPbBr₃, *J. Phys. Chem. Lett.* 8 (2) (2017) 489–493.
- [37] J.L. Li, J.X. Yang, T. Wu, S.H. Wei, Formation of DY center as n-type limiting defects in octahedral semiconductors: the case of Bi-doped hybrid halide perovskites, *J. Mater. Chem. C* 7 (14) (2019) 4230–4234.
- [38] T.T. Shi, W.J. Yin, F. Hong, K. Zhu, Y.F. Yan, Unipolar self-doping behavior in perovskite CH₃NH₃PbBr₃, *Appl. Phys. Lett.* 106 (10) (2015) 103902.
- [39] Y. Kang, C.G. Van de Walle, Electrical compensation mechanism in fluorine-doped SnO₂, *Appl. Phys. Lett.* 111 (15) (2017) 152107.
- [40] J. Lee, S. Han, Thermodynamics of native point defects in α -Fe₂O₃: an ab initio study, *Phys. Chem. Chem. Phys.* 15 (43) (2013) 18906–18914.